



**HAL**  
open science

# Three-scale analysis of the permeability of a natural shale

C. A. Davy, P. M. Adler

► **To cite this version:**

C. A. Davy, P. M. Adler. Three-scale analysis of the permeability of a natural shale. *Physical Review E*, 2017, 96, 10.1103/PhysRevE.96.063116 . insu-03746416

**HAL Id: insu-03746416**

**<https://insu.hal.science/insu-03746416>**

Submitted on 2 Sep 2022

**HAL** is a multi-disciplinary open access archive for the deposit and dissemination of scientific research documents, whether they are published or not. The documents may come from teaching and research institutions in France or abroad, or from public or private research centers.

L'archive ouverte pluridisciplinaire **HAL**, est destinée au dépôt et à la diffusion de documents scientifiques de niveau recherche, publiés ou non, émanant des établissements d'enseignement et de recherche français ou étrangers, des laboratoires publics ou privés.

**Three-scale analysis of the permeability of a natural shale**

C. A. Davy\*

*Laboratoire de Mécanique de Lille (LML), FRE CNRS 3723 and Ecole Centrale de Lille, CS 20048, F-59651 Villeneuve d'Ascq Cedex, France*

P. M. Adler†

*UPMC METIS, Boîte 105, 4 place Jussieu, 75252 Paris cedex 05, France*

(Received 7 May 2017; published 26 December 2017)

The macroscopic permeability of a natural shale is determined by using structural measurements on three different scales. Transmission electron microscopy yields two-dimensional (2D) images with pixels smaller than 1 nm; these images are used to reconstruct 3D nanostructures. Three-dimensional focused ion beam–scanning electron microscopy (5.95- to 8.48-nm voxel size) provides 3D mesoscale pores of limited relative volume (1.71–5.9%). Micro-computed tomography (700-nm voxel size) provides information on the mineralogy of the shale, including the pores on this scale which do not percolate; synthetic 3D media are derived on the macroscopic scale by a training image technique. Permeability of the nanoscale, of the mesoscale structures and of their superposition is determined by solving the Stokes equation and this enables us to estimate the permeabilities of the 700-nm voxels located within the clay matrix. Finally, the Darcy equation is solved on synthetic 3D macroscale media to obtain the macroscopic permeability which is found in good agreement with experimental results obtained on the centimetric scale.

DOI: [10.1103/PhysRevE.96.063116](https://doi.org/10.1103/PhysRevE.96.063116)**I. INTRODUCTION**

Claystones and shales are low-permeability sedimentary rocks. Due to this property, they are potential host rocks for the long-term repository of long-lived and medium- to high-activity nuclear waste in several industrialized countries [1]. Understanding and predicting fluid transport through these geomaterials is key to ensuring an adequate retention of radionuclides, together with a thoroughly designed engineered barrier. Alternatively, shales may host natural gas [2], whose recovery can be enhanced through the understanding and prediction of fluid transport.

Shale pores are located within the clay matrix or at its interface with nonporous minerals [3–11]. They are characterized by a bimodal pore size distribution, with one main peak of a few nm size, and the second of a few tens of nm size [2,8] (unless otherwise stated, in this contribution, pore size refers to pore diameter and not radius). These pores, located in the clay matrix, most likely dominate the flow and transport properties [6,8–10]. During sedimentation and compaction, clay minerals are deposited along preferred orientations; it is also expected that the pore space geometry is anisotropic [12], as are the transport properties of the shale [13].

Characterizing the three-dimensional (3D) pore structure of shales is a preliminary to an accurate prediction of their transport properties from 3D numerical simulations (permeability tensor). To our knowledge, due to the broad range of pore sizes involved, and to the inherent heterogeneity of these natural materials (which comprise swelling clay, soft and hard minerals), 3D predictions of the shale transport properties from the nano- to the macroscale have not been undertaken yet and this is the major purpose of this paper.

The 3D characterization of the pore space has been the subject of a number of studies. At least for the natural shale (NS) studied herein, as well as for the Swiss Opalinus clay [4–6] and for several Northern American shales [2], at present, no single technique provides a full overview of its porosity for bulk matter on the centimetric scale and above. A combination of different techniques is recommended. These techniques are either direct, i.e., imaging techniques, or indirect, i.e., they require a simplified model to derive pore characteristics. Indirect techniques often rely either on gas adsorption (for the smallest nanoscopic pores only) or on capillary intrusion of a liquid fluid (for plurinometric to millimetric pores only). The sample preparation technique, involving small or powdered samples, may also limit the applicability to bulk matter.

Direct 3D imaging provides all the necessary geometrical parameters, but the physical size of the region of interest, having fixed dimensions in terms of its number of voxels, reduces with decreasing voxel size. This requires a characterization in a statistical sense, by involving the largest possible number of imaged zones at each scale. Currently, for NS, x-ray micro-computed tomography (micro-CT) provides data for the 3D pore space down to a 700-nm voxel size [7]. This is insufficient to predict transport because no percolating porosity is recorded at this scale, although the analyzed sample is representative of a “macroscopic” structure (up to about 180- $\mu$  wide), where all mineral phases (mainly a clay matrix, carbonates, tectosilicates, and heavy minerals) are present [7]. Higher resolutions are available with focused ion beam–scanning electron microscopy (FIB-SEM) down to 10- to 20-nm voxel size, and transmission electron microscopy (TEM) or scanning transmission electron microscopy (STEM) techniques, down to below 1-nm pixel or voxel size [6,8–10].

In this research, synthetic images are derived on the macroscopic scale by training image (TI) techniques [14,15] from micro-CT data for NS [7]. At the mesoscale, also for NS, four percolating FIB-SEM samples are available from

\* catherine.davy@centralelille.fr

† pierre.adler@upmc.fr

Ref. [9], and at the nanoscopic scale, up to eight TEM images are available from Ref. [8].

The major purpose of this paper is to use these data in order to determine the overall permeability of natural shale NS by three successive upscalings. All calculations are performed using the assumption that the medium is continuous at all scales. For fluid transport by convection, this is valid down to a few-nm pore size whenever a simple liquid is considered as shown repeatedly (cf. Ref. [16] for a review). No interactions with the solids, nor any phenomenon specific to flow (e.g., slippage on the pore walls or Brownian motion), need to be accounted for. Whenever a percolating pore structure is known (at both the meso- and nanoscales), the Stokes equation is solved by a Lattice Boltzmann Method (LBM) [17]. On the larger macroscopic scale, when a local permeability field is available, the macroscopic permeability is deduced by solving the Darcy equation [18]. In the latter case, the clay matrix is the only volume assumed permeable, together with the nonpercolating pore volume (0.5%); all other minerals are nonporous, and no interfacial porosity is accounted for.

The paper is organized as follows. Section II briefly recalls the experimental measurements, which were performed in order to characterize the clay matrix structures on the nano-, meso-, and macroscales. The numerical techniques are also briefly presented. Reconstruction techniques on the nano- and on the macroscales are presented as well as the numerical solutions of the Stokes and of the Darcy equations.

The major results are gathered in Sec. III. Permeabilities on the nanoscale (Sec. A) and on the mesoscale (Sec. B) are first determined. Then, permeabilities of combinations of nano- and mesoscale structures are calculated in Sec. C. These intermediate values are used to determine the macroscopic permeability by solving the Darcy equation on a configuration derived from micro-CT measurements in Sec. D. These data and their comparison to permeability measurements on the macroscale are discussed in Sec. IV. Finally, concluding remarks are given in Sec. V.

## II. METHODS

### A. Experimental

First, the experimental permeability  $K_{\text{exp}}$  was measured at 20°C in Ref. [8] with ethanol, whose molecular size is 0.469 nm. The samples had a diameter of 37 mm and a height ranging between 10 and 30 mm. Each sample was confined at a hydrostatic pressure of 12 MPa (representative of the *in situ* major principal stress) and injected with ethanol at a given pressure gradient. Results detailed in Ref. [8] and references therein can be summarized as follows:

$$8 \times 10^{-21} \leq K_{\text{exp}} \leq 6 \times 10^{-20} \text{ m}^2. \quad (1)$$

These experimental permeability values  $K_{\text{exp}}$  depend on the considered core, i.e., they are attributed to variations in the natural shale mineralogical composition.

For FIB-SEM imaging, two shale samples of core reference EST26095 and EST27405 are used. The latter is simply dried at 60°C until constant mass. In contrast, the EST26095 sample is oven dried at 80°C and impregnated with a low-viscosity methyl methacrylate resin (MMA) [7,19]. MMA shows excellent pore filling ability [19] due to a small molecule

size (0.19 nm<sup>3</sup>) and a very low viscosity (of about 0.6 cP at 20°C), which is smaller than that of water (1.0020 cP at 20°C). Following impregnation, MMA is polymerized (into PMMA) using  $\gamma$  radiation provided from a <sup>60</sup>Co source [19]. For further sample polishing, PMMA limits the hardness difference between the soft clay matrix and the hard minerals (tectosilicates, carbonates, and heavy metals). Proper flatness is also achieved more smoothly than without any impregnation. On the whole, PMMA aims at limiting sample damage and microcracking.

For TEM imaging, a shale sample of core reference EST25679 is also dried at 80°C and impregnated with PMMA with the same method as for the EST26095 sample. The EST25679 sample is thinned to several tens of microns, prior to being ion milled using a Gatan Duomill apparatus, with a liquid nitrogen-cooled specimen holder to limit sample damage, until sample edges show electron transparency. This corresponds to thicknesses below 100 nm.

All grayscale images acquired by FIB-SEM and TEM are filtered, thresholded, and segmented with ImageJ software to distinguish between the pores and the solids. For FIB-SEM, the  $z$  axis is the direction perpendicular to imaging (it is the direction for slicing the sample at 10- to 20-nm thicknesses), whereas each image is in an  $xy$  plane. Full details on the procedures are given in Refs. [8,9].

### B. The main measurements

For NS, the average macroscopic porosity is measured by different means [11,20] with an average of 18%  $\pm$  4. Its value mainly depends on the location of the sample in the geological layer. Moreover, at least three distinct scales can be distinguished, i.e., a macroporosity (for pores bigger than 700 nm), a mesoporosity (for pores bigger than 10–20 nm and up to 700–800 nm), and a nanoporosity (for pores bigger than 0.36 nm and up to 10–20 nm).

#### 1. Macroporosity

Figure 1(a) is the starting point of the simulation on the macroscopic level. The original measurements have been performed by Ref. [7], with a voxel size of 700 nm and a total

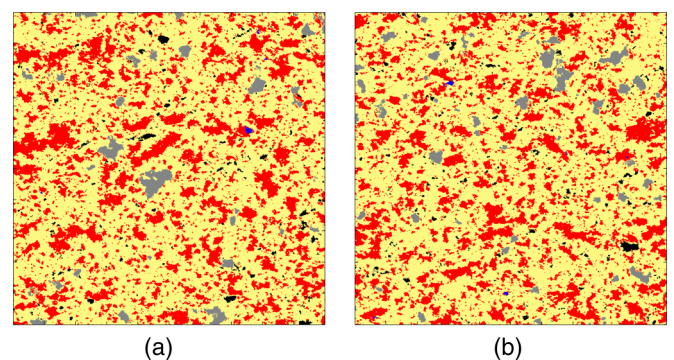


FIG. 1. Macroscale. (a) Training image from Ref. [7]. (b) Cross section of the simulated sample. Color code: black (macroscopic isolated pore), yellow (clay matrix), gray (tectosilicates), red (carbonates), and deep blue (heavy minerals). Both samples measure 1 mm  $\times$  1 mm.

TABLE I. Overview of the 3D FIB-SEM samples (1).

Sample	EST2-EST27405-1	EST3-EST27405-2
Sample orientation wrt. bedding planes	Perpendicular	Perpendicular
Voxel size (nm <sup>3</sup> )	8.49×10.78×10	5.94×7.54×10
Volume (μm <sup>3</sup> )	6.55×7.97×1.03 (=53.8)	3.99×5.95×1.17 (=27.8)
Porosity-Yen algorithm (%)	2.83	4.89
Surface connected orientation	<b>z</b>	<b>z</b>
Connected porosity (%)	0.89	1.61

volume of 180 μ width. The medium is composed of several mineral types represented by different colors (clay matrix, tectosilicates, carbonates, and heavy minerals). The overall porosity at that so-called macroscopic scale is 0.5%. The pores are not connected. Therefore, the macroscopic permeability due to these pores only is equal to zero. This requires us to go one scale down at least in order to provide a percolating pore network.

In the following, the three minerals that are tectosilicates, carbonates, and heavy minerals are gathered into a single phase whose permeability is zero; the volume fraction of these three phases all together is equal to 39.5%. The phase of interest, composed by the clay matrix, has an overall volume fraction of 60%.

## 2. Mesoporosity

The main properties of the five available FIB-SEM samples are given in Tables I and II. Their volumes range between 27.8 and 146.7 μm<sup>3</sup>, and their total porosity with this method ranges between 1.71 and 5.9%. The voxel is parallelepipedic and not cubic, with its smallest dimension ranging between 5.94 nm (for EST3-EST27405-2) and 8.48 nm (for EST2-EST27405-1, EST0-EST26095-1, EST1-EST26095-2, and EST4-EST26095-3). The total number of voxels varies between 48.7×10<sup>6</sup> (for EST1-EST26095-2) and 80.3×10<sup>6</sup> (for EST0-EST26095-1).

The reanalysis of the five available volumes with the code described by Ref. [21] shows that only four are percolating, three along the *z* axis and one along the *y* axis. The initial representations of these four percolating samples are given in Fig. 2. A connected pore network, devoid of cracks, is

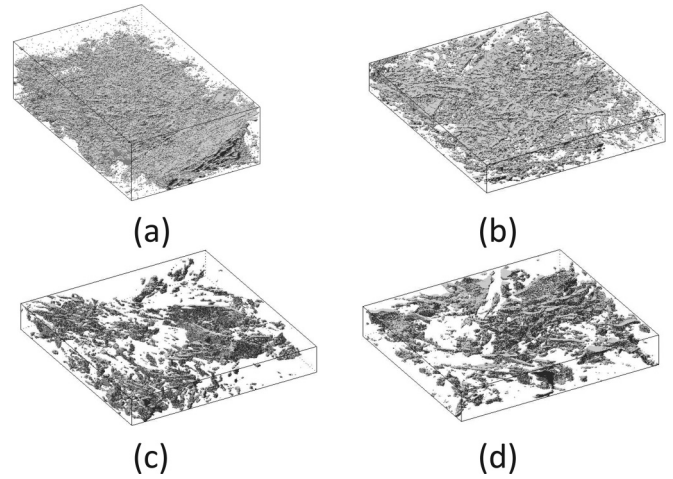


FIG. 2. Initial measurements on the mesoscale obtained by FIB-SEM. Three-dimensional data images are for (a) EST0-EST26095-1, (b) EST1-EST26095-2, (c) EST2-EST27405-1, and (d) EST3-EST27405-2.

obtained for two samples of five only (EST0-EST26095-1 along *y* and EST1-EST26095-2 along *z*), while the pore network is connected through cracks for two other samples of five (EST2-EST27405-1 and EST3-EST27405-2) [9].

## 3. Nanoporosity

Figure 3(a) shows an example of a TEM image. Several subsamples of this image are taken within the clay aggregates. These subsamples display nanoscopic pores of the clay matrix (from about 2 nm and up to several hundreds of nm; see Table III). The bigger pores also visible in this image (e.g., between clay aggregates) are assumed to be identified by FIB-SEM (down to 10- to 20-nm size) or micro-CT (down to 700 nm). In Figs. 3(b)–(d), several segmented TEM crops are presented, and for T10-1, the image before and after segmentation is given. The pixel size varies from one image to the other, between 0.36 nm and 1.04 nm, depending on the TEM image resolution. For all the crops considered in Ref. [8], the image area ranges between 18.5×10<sup>3</sup> and 41.0×10<sup>3</sup> nm<sup>2</sup> for pixel numbers of between 25.5×10<sup>3</sup> and 262×10<sup>3</sup>. Porosity ranges between 10.1 and 25.2%, with an average value of 14.9% and a median of 14.2%. Moreover, the ratio between longest and shortest axis of an inscribed ellipsoid, i.e., the pore elongation, is of about 10, with a median

TABLE II. Overview of the 3D FIB-SEM samples (2).

Sample	EST0-EST26095-1	EST1-EST26095-2	EST4-EST26095-3
Orientation wrt. bedding planes	Parallel	Parallel	Parallel
Voxel size (nm <sup>3</sup> )	8.48×10.77×20	8.48×10.77×20	8.49×10.78×20
Volume (μm <sup>3</sup> )	6.55×5.21×4.30(=146.7)	6.30×6.99×2.02(=88.9)	4.50×6.22×3.98(=111.4)
Porosity -Yen algorithm (%)	1.71	5.9	5.21
Percolating direction	<b>y</b>	<b>z</b>	None
Connected porosity (%)	2.25	2.14	0

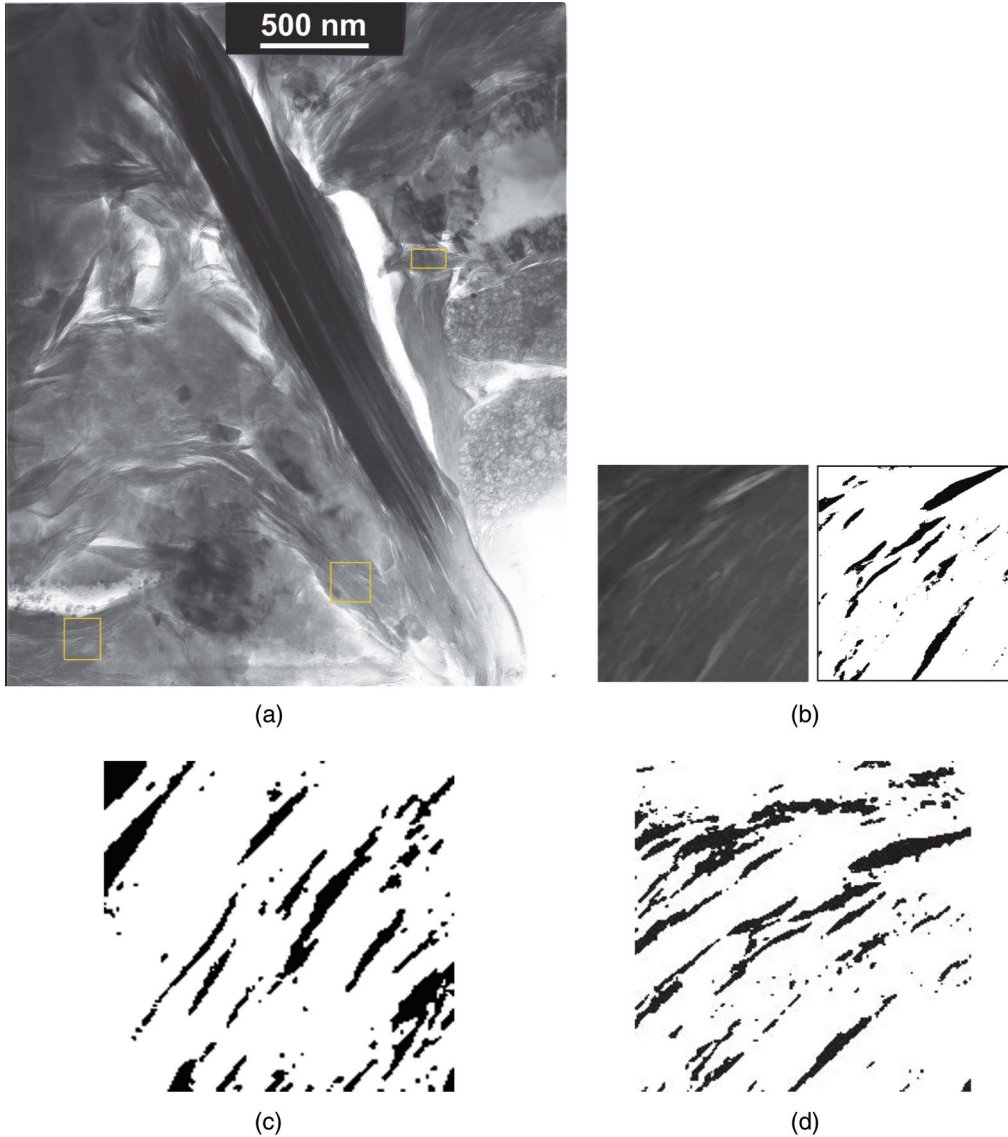


FIG. 3. (a) Example of a nanoscale image obtained by TEM on the natural shale of this study, and different crops located in the clay aggregates. (b) Crop T10-1 (before and after segmentation) has the smallest porosity of 10.1% (pixel size 0.36 nm); (c) Crop T08-2 has an intermediary porosity of 14.2% (pixel size 0.85 nm); (d) Crop T09-2 has the largest porosity of 25.2% (pixel size 1.04 nm).

value of 8.3 (i.e., 50/6). In 3D, by analogy with the 3D STEM image of Opalinus clay presented in Ref. [6], it is assumed that they have the shape of oblates.

It might be interesting to note that the FIB-SEM measurements are nicely complemented by TEM. Whereas FIB-SEM has lower pore size limits of 10–20 nm, 2D TEM images have pore sizes ranging from 0.7 to 20 nm (as determined by 2D

ellipse fitting in ImageJ), with percentages of pores smaller than 20 nm ranging between 99.3 and 100%.

**C. Conventions and notations**

Three scales are distinguished in the analysis. The first two correspond to the nano- and the mesoscales, which are approximately equal to 2 and 20 nm. The macroscopic scale is of the order of the size of the cross section displayed in Fig. 1, i.e., 1 mm (voxel size 700 nm). It is derived from micro-CT data and corresponds to the smallest scale, where all different solid phases identified for NS are present.

Quantities such as porosity  $\epsilon$  and permeability  $K$  are given the subscripts  $n$ ,  $m$ ,  $M$ , and MA when they are relative to the nanostructure ( $n$ ), to the mesostructure ( $m$ ), to local variations at the macrostructure scale ( $M$ ), or as an average over the macrostructure considered as a homogeneous medium (MA).

TABLE III. Characteristics of the TEM images used for the numerical simulations of transport.

Sample	Pixel size (nm <sup>2</sup> )	Sample size (nm <sup>2</sup> )	Crop size (nm <sup>2</sup> )	Porosity (%)
T10 <sub>1</sub>	0.36×0.36	658×799	176×193	10.2
T08 <sub>2</sub>	0.85×0.85	1540×1886	140×132	14.2
T09 <sub>1</sub>	1.04×1.04	1903×2329	160×240	25.2

**D. Numerical**

**1. Reconstruction on the nanoscale**

On the nanoscale, in the absence of 3D images, the pore structure is reconstructed from the 2D TEM images, with the same porosity and the same correlation function, by using a technique based on truncated Gaussian fields [22]. A random and discrete field  $Z(\mathbf{x})$  is derived from a Gaussian field  $X(\mathbf{x})$ , which is first correlated and then thresholded.

The general technique goes as follows. A Gaussian and uncorrelated field  $X(\mathbf{x})$  is generated at the center of each elementary cube. The independent random variables  $X(\mathbf{x})$  are assumed to be normally distributed with a mean equal to 0 and a variance equal to 1. A Gaussian field  $Y(\mathbf{x})$  with a given correlation function  $R_Y(\mathbf{u})$  is derived from the field  $X(\mathbf{x})$  by a Fourier transform technique. Finally, the field  $Y(\mathbf{x})$  is thresholded and yields a discrete field  $Z(\mathbf{x})$ ; the threshold is such that the average value of  $Z(\mathbf{x})$  is equal to the desired porosity  $\epsilon_n$ . By construction, the 3D pore volume at the nanoscopic scale is spatially periodic along the three dimensions of space.  $R_Y(\mathbf{u})$  may be derived from  $R_Z(\mathbf{u})$  either measured on thin sections [22] or given by some analytical formula [23].

The nanoscale pictures displayed in Fig. 3 are not isotropic. In order to generate flat-shaped nanopores, a correlation function of the following form is used for the Gaussian field  $Y(\mathbf{x})$ :

$$R_Y(\mathbf{u}) = R_Y(u_x, u_y, u_z) = \exp\{-(u_x/l_x)^2 - (u_y/l_y)^2 - (u_z/l_z)^2\}, \quad (2a)$$

where  $l_x \ll l_y = l_z$ . It is assumed that the  $y$  and  $z$  axes are equivalent. In the rest of this paper, the three correlation lengths are equal to

$$l_x = 6a, \quad l_y = l_z = 50a, \quad (2b)$$

where  $a$  is the size of the cubic voxels, which is taken to be equal to 2.12 nm. Therefore, in nm,

$$l_x = 12.72 \text{ nm}, \quad l_y = l_z = 106 \text{ nm}. \quad (2c)$$

One should also note that the pixel size of the original 2D TEM images is not 2.12 nm. However, in order to allow for the superposition with the mesoscale pore structures (where the voxel size is generally of 8.48 nm, i.e., 4 times the latter value), the 3D synthetic TEM images are scaled by using Eqs. (2a) and (2b), which account for the original TEM images characteristics as detailed above. In the following, the superposition of the mesoscale structure of EST3-EST27405-2 (smallest voxel size of 5.94 nm) to the nanoscale pore structure is not undertaken. It is assumed that it would yield similar results to those presented hereafter. Some calculations are also undertaken by generating a 3D nanoscale pore structure with  $a = 8.48$  nm.

An example of 3D reconstruction is given in Fig. 4. It is mostly composed of vertical oblates which are partly connected to one another in all the directions of space. Cross sections are also displayed; Figs. 4(b) and 4(d) are very similar to the ones measured given in Fig. 3.

**2. Sample rediscrretization and percolating components**

Since the original voxels are not cubic, several operations were performed to prepare the measured samples to flow

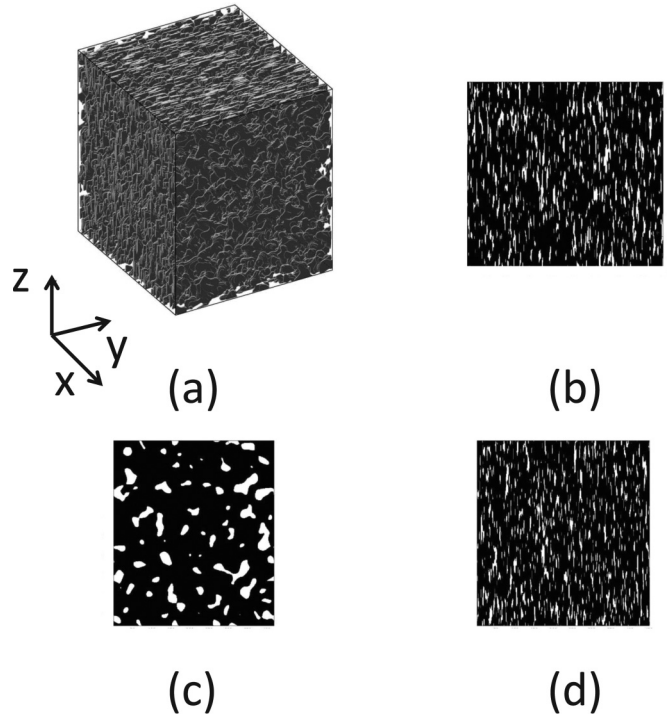


FIG. 4. Reconstruction of the nanoscale structure. (a) A three-dimensional nanostructure with  $l_x=6a$   $l_y=l_z=50a$  and  $\epsilon=0.142$ ; this sample percolates along the three axes. Cross sections of the simulated sample: (b)  $xy$  plane, (c)  $yz$  plane, and (d)  $zx$  plane.

calculations; they are illustrated in Fig. 5 on the example of EST3-EST27405-2. First, the percolating part of the samples, when it exists, was determined by the algorithm described in Ref. [21]. The samples percolate along a single direction, only which varies from sample to sample. Since the LBM code described in Section 2.4.3 only operates on cubic voxels, the parallelepipedons are rediscrretized into cubes of size 5.94

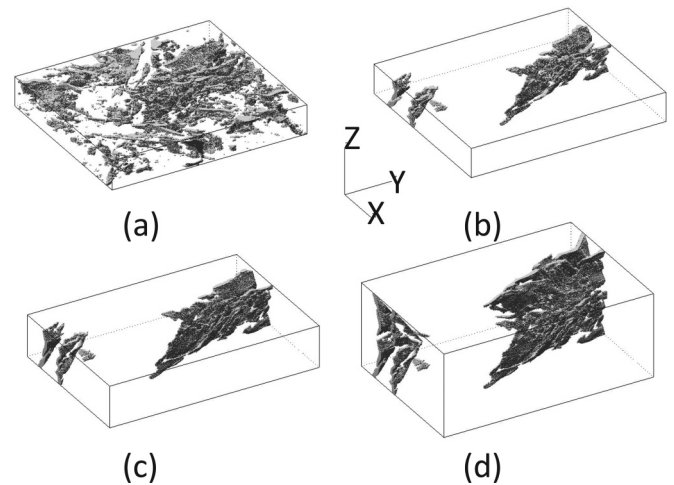


FIG. 5. Example of processing of the initial FIB-SEM sample EST3-EST27405-2. (a) The initial sample. (b) The percolating part of the pore structure is retained. (c) The parallelepipedic voxels are rediscrretized into cubes. (d) The mirror image of the percolating pore structure is added along a percolating direction, here the  $z$  direction.

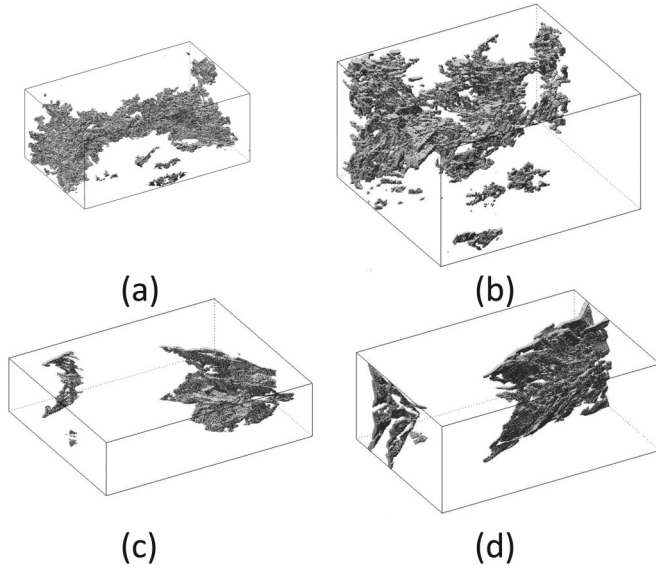


FIG. 6. Mesoscale. The four percolating components of the initial samples displayed in Fig. 2. Data are for (a) EST0-EST26095-1 (cubic voxel size 8.48 nm; percolation along the  $y$  axis), (b) EST1-EST26095-2 (cubic voxel size 8.48 nm; percolation along the  $z$  axis), (c) EST2-EST27405-1 (cubic voxel size 8.48 nm; percolation along the  $z$  axis), and (d) EST3-EST27405-2 (cubic voxel size 5.94 nm; percolation along the  $z$  axis). The last two samples percolate through microcracks only.

nm (or 8.48 nm for EST0-EST26095-1, EST1-EST26095-2, and EST2-EST27405-1). Finally, the mirror image of the sample is added along the percolating direction; this addition diminishes the bias introduced by the boundary conditions in the calculated permeability. It is clear that the order of these operations can be modified at will.

The four samples are processed by this series of operations and the final results with cubic voxels are shown in Fig. 6.

### 3. Permeability derived from the Stokes equation

Whenever the pore structure is available, the corresponding permeability can be derived by solving the Stokes equation. This procedure is applied to the nanoscale and mesoscale structures and to their superposition.

As mentioned in the Introduction, the use of the Stokes equation in the nanoscale structure is questionable, because the continuum assumption could break down. However, the characteristic dimensions of the nanopores where the calculations are performed are given by (2c); they are more than 25 times larger than the ethanol molecule; they are also larger than 10 nm. Moreover, because of the neutral nature of ethanol, electrical effects are negligible and the Stokes equation does not need to be completed by electrical forces. Therefore, for a simple liquid such as ethanol, the permeability obtained by the Stokes equation can be safely compared to the experimental measurements (cf. Ref. [16] and references therein).

This equation is usually expressed as

$$-\nabla p + \mu \nabla^2 \mathbf{v} = 0, \quad \nabla \cdot \mathbf{v} = 0 \quad \text{in } V_p, \quad (3)$$

where  $p$  and  $\mathbf{v}$  denote pressure and velocity, respectively;  $\mu$  is the fluid viscosity;  $V_p$  is the pore volume.

This system should be supplemented by boundary conditions. Assuming that the solid matrix is impermeable, the fluid velocity should vanish on the solid surface  $S_p$ , which limits the pore space

$$\mathbf{v} = 0 \quad \text{on } S_p. \quad (4)$$

In addition, spatially periodic boundary conditions are applied at the lateral boundaries of the sample. The driving force is a macroscopic pressure gradient  $\overline{\nabla p}$  imposed on the sample.

The seepage velocity  $\overline{\mathbf{v}}$  is the average of the local velocity over the pore volume and it is proportional to  $\overline{\nabla p}$ ,

$$\overline{\mathbf{v}} = \frac{1}{V_p} \int_{V_p} \mathbf{v} d^3 \mathbf{x} = -\frac{1}{\mu} \mathbf{K} \cdot \overline{\nabla p}. \quad (5)$$

The components of the permeability tensor  $\mathbf{K}$  are denoted by the names of the corresponding axes, for instance, the diagonal component along the  $x$  axis is noted by  $K_{xx}$ .

The numerical resolution of the Stokes equation can be done in different ways, namely a classical computational fluid dynamic (CFD) technique applied to cubic voxels [22], a lattice Boltzmann model [17] and the finite-volume technique applied to tetrahedra [24].

In this contribution, the second technique is applied since the corresponding code is parallel and thus significantly faster for the sample volumes considered (in tens of million voxels). According to the standard terminology, it is a D3Q19 code working in three dimensions with 19 velocities. For a better precision, the model is TRT, i.e., with two relaxation times. The classical bounce-back condition is used at the solid interface. More details can be found in Ref. [17].

It should be emphasized that in this LBM code the fluid is treated as a continuum in contrast with some more elaborate versions such as in Ref. [25].

Needless to say, the LBM code has been compared in the past to the two other techniques just mentioned. The results for plane Poiseuille flows can be briefly summarized. Whatever the width  $b$  of the channel, the LBM and the second-order CFD codes agree perfectly well. For  $b = 5$  voxels, the difference with the analytical solution is smaller than 2%. Perhaps, still more remarkable, their common difference with the analytical solution is equal to 11% for  $b = 2$  voxels.

Permeabilities, which have the dimension of a length squared, are usually made dimensionless by the voxel size  $a$  and are denoted by a prime

$$K' = \frac{K}{a^2}. \quad (6)$$

Since the algorithm assumes a spatially periodic structure, each sample is completed by its mirror image along the direction under consideration. This detail will be made clear in each calculation.

### 4. Reconstruction on the macroscopic scale

Consider the porous medium displayed in Fig. 1(a). This sample may be two or three dimensional and it contains several minerals in addition to pores. Such a sample is called a TI, whether it is two or three dimensional.

The main objective of Ref. [14] was to generate a simulated medium (SM) based on such TIs. Following Ref. [22], a phase

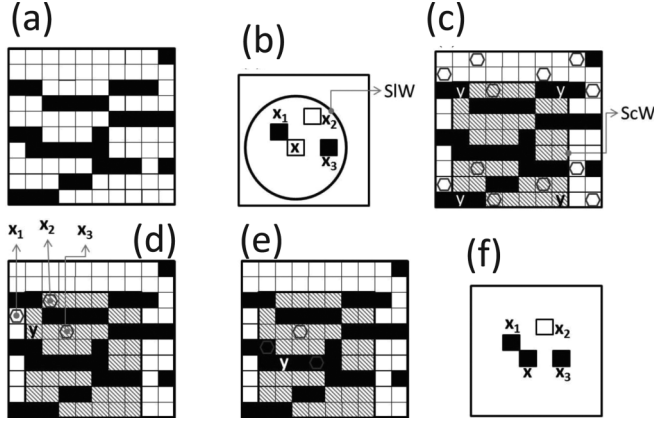


FIG. 7. Principle of the training image (TI) algorithm. Panel (a) is the TI with black and white pixels. Panel (b) is the simulated medium (SM); the three points  $x_1, x_2, x_3$  are known and the fourth one  $x$  has to be determined. Panel (c) provides the Search Window in gray where the point  $y$  is necessarily located. (d) In the TI, for this choice of  $y$ , the three points  $x_1, x_2, x_3$  are white; therefore,  $y$  has to be chosen differently. (e) For this choice of  $y$ , the three points  $x_1, x_2, x_3$  have the right gray level when compared to (b); therefore, the black value is chosen for  $x$ . (f) Assign the black value of  $y$  in (e) to point  $x$  in the SM.

function  $Z(\mathbf{x})$  can be defined at each point  $\mathbf{x}$  of the medium. Suppose that  $N_p$  different phases (possibly including the pore space) can be distinguished in the medium. Then, at each pixel or voxel centered at  $\mathbf{x}$  and occupied by phase  $i_p = 1, \dots, N_p$ ,  $Z(\mathbf{x})$  is defined as

$$Z(\mathbf{x}) = i_p. \quad (7)$$

The methodology to generate SM was devised by Ref. [15] and is briefly described now with the help of Fig. 7. The TI is displayed in (a); it has two colors, black and white. Suppose that three points  $x_1, x_2, x_3$  are known in the SM and that one wants to determine the value (or the color) of a fourth one  $x$  as indicated in Fig. 7(b). Now, let us choose a point  $y$  at random in the TI and look at the values of three points  $x_1, x_2, x_3$  in the TI which occupy the same relative positions with respect to  $y$  in the TI as with respect to  $x$  in the SM.

First, a remark can be made to save some computer time. Because of the relative positions of the known points ( $x_1, x_2, x_3$ ) and of the fourth point  $y$  to be scanned,  $y$  is necessarily located in a portion of the TI which is called the Search Window (ScW) [see the gray zone in Fig. 7(c)].

Second, find in the TI a configuration where the three points  $x_1, x_2, x_3$  have the same relative positions and the same colors as in the SM. This is done by choosing a point  $y$  at random in the ScW (which corresponds to the point to fill) and by looking at its three neighbors (they correspond to the points 1–3) in the same relative positions as in the SM. In Fig. 7(d), the point to fill is indicated by  $y$ ; the three points  $x_1, x_2, x_3$  are all white and therefore do not have the right color. Then, let us make a different choice in the TI; in Fig. 7(e), the three points have the right gray level and the value black in the TI is chosen for point  $y$ . The corresponding choice is indicated in Fig. 7(e). When no match is found at the beginning of the process, another choice of points  $x_1, x_2, x_3$  is made; towards

the end, the fourth point is chosen according to the remaining probabilities.

When this step is completed, the process is iterated and the SM progressively filled.

The 3D macroscopic sample, whose cross section is displayed in Fig. 1(b), was generated by using this technique.

### 5. Permeability on the macroscopic scale

On the macroscopic scale illustrated in Fig. 1, the medium is no longer composed of solid and pores. Rather, it is a continuum with a locally variable permeability  $K_M(\mathbf{x})$  yielding the local macroscopic permeability. For instance, in Fig. 1(b), the voxel permeability depends on the mineral present in this voxel as detailed in Sec. 2.1. Then, the local seepage velocity  $\bar{v}_M$  is related to the local pressure gradient by Darcy's law,

$$\bar{v}_M = -\frac{K_M(\mathbf{x})}{\mu} \nabla p. \quad (8a)$$

Since for an incompressible fluid the seepage velocity satisfies the continuity equation, one has

$$\nabla \cdot (K_M(\mathbf{x}) \nabla p) = 0. \quad (8b)$$

Usually, the total block of volume  $V$  is submitted to a macroscopic pressure gradient  $\nabla p$ . The resulting macroscopic seepage velocity  $\bar{v}$  is defined as follows, and it is related to  $\nabla p$  by the macroscopic permeability  $\mathbf{K}_{MA}$ ,

$$\bar{v} = \frac{1}{V} \int_V \bar{v}_M d^3 \mathbf{x} = -\frac{1}{\mu} \mathbf{K}_{MA} \cdot \nabla p. \quad (9)$$

The elliptic equation (8b) is discretized by the so-called box integration method [26] and the resulting linear system is solved by a conjugate gradient method, as detailed in Ref. [18].

## III. RESULTS

### A. Permeability on the nanoscale

Two sets of nanoscale structures were generated, which follow the Gaussian correlation function (2) for five values of porosity  $\varepsilon_n$ . These two sets only differ by the size of the generated media. For set 1, one has  $N_{CX} = 451$  pixels,  $N_{CY} = 419$  pixels,  $N_{CZ} = 484$  pixels (i.e., 91.5 million pixels) while for set 2  $N_{CX} = N_{CY} = N_{CZ} = 400$  pixels (i.e., 64 million pixels). The generated samples are spatially periodic. The directions  $y$  and  $z$  are expected to be statistically equivalent since the correlation lengths  $l_y$  and  $l_z$  are equal (2b). Results are gathered in Table IV.

The samples for the lowest value of the porosity  $\varepsilon_n = 10.2\%$  do not percolate, while the samples for  $\varepsilon_n = 13.0\%$  (and more) percolate. As expected, permeability increases with porosity. The discrepancies between the two sets for the same porosity are always small; however, it is interesting to note that they decrease when  $\varepsilon_n$  increases; it is a well known fact in percolation theory that statistical fluctuations are important close to the percolation threshold. Of course, the permeabilities are anisotropic;  $K_{nyy}$  and  $K_{nzz}$  are statistically equivalent, while  $K_{nzz}$  is consistently greater than  $K_{nxx}$ . Since the results for  $K_{nzz}$  are very close for sets 1 and 2, it was not found useful to redo them for the other axes.

TABLE IV. Dimensionless permeabilities on the nanoscale. Data are for:  $a = 2.12$  nm; set 1:  $N_{CX} = 451$ ,  $N_{CY} = 419$ ,  $N_{CZ} = 484$ ; set 2:  $N_{CX} = N_{CY} = N_{CZ} = 400$ .

Porosity $\varepsilon_n$	Percolation axis	Set 1			Set 2
		$K'_{nxx}$	$K'_{nyy}$	$K'_{nzz}$	$K'_{nzz}$ for $400^3$
0.102	None	–	–	–	
0.130	$y, z$	0	$0.850 \times 10^{-3}$	$0.65 \times 10^{-3}$	$0.677 \times 10^{-3}$
0.142	$x, y, z$	$0.487 \times 10^{-2}$	$0.124 \times 10^{-2}$	$= K'_{nyy}$	$0.137 \times 10^{-2}$
0.200	$x, y, z$	$0.686 \times 10^{-2}$	$0.138 \times 10^{-1}$	$= K'_{nyy}$	$0.132 \times 10^{-1}$
0.252	$x, y, z$	$0.802 \times 10^{-2}$	$0.404 \times 10^{-1}$	$= K'_{nyy}$	$0.392 \times 10^{-1}$

Finally, the data of Table IV can be converted into dimensional values; the lower and higher values of permeability are determined and yield the inequalities

$$3 \times 10^{-21} \leq K_{nxx}, \quad K_{nyy} \simeq K_{nzz} \leq 1.8 \times 10^{-19} \text{ m}^2. \quad (10)$$

On the nanoscale, permeability varies by almost two orders of magnitude depending on the flow direction.

### B. Permeability on the mesoscale

On the mesoscale, percolation of the FIB-SEM pore volumes occurs only along a single direction as already pointed out in Section 2, either along  $z$  (for EST1-EST26095-2, EST2-EST27405-1, and EST3-EST27405-2) or  $y$  (for EST0-EST26095-1). Each sample is mirrored with respect to the plane perpendicular to the percolating direction. The mesoscopic permeability  $K_m$  varies between  $2.8 \times 10^{-20} \text{ m}^2$  and  $1.20 \times 10^{-18} \text{ m}^2$ , depending on the nature of the percolating volume (Table V). As discussed in Sec. 3.2, the largest values of  $K_m$  obtained with EST2-EST27405-1 and EST3-EST27405-2, correspond to percolating volumes identified as cracks.

It is interesting to note that the largest value  $1.8 \times 10^{-19} \text{ m}^2$  of  $K_n$  is larger than the smallest value  $2.8 \times 10^{-20} \text{ m}^2$  of  $K_m$ . This means that the nanoscale porosity can have a significant contribution to the overall permeability.

### C. Superposition of the nanoscale and of the mesoscale pore structures

The current discretization voxels of the nano- and mesoscales are 2.12 and 8.48 nm. A rediscrretization of the full mesoscale structures with  $a = 2.12$  nm would yield very large data sets that we cannot presently process. Therefore, it was chosen to work with various subsamples of the mesoscale structures. An example of the effect of a coarse discretization with  $a = 8.48$  nm will also be provided.

TABLE V. Permeability results of the mesoscale.

Sample	$a$ (nm)	$K'_{myy}$	$K'_{mzz}$	$K_m$ ( $\text{m}^2$ )
EST0-EST26095-1	8.48	$8.38 \times 10^{-4}$	0	$6.03 \times 10^{-20}$
EST1-EST26095-2	8.48	0	$3.89 \times 10^{-4}$	$2.80 \times 10^{-20}$
EST2-EST27405-1	8.48	0	$37.9 \times 10^{-4}$	$27.3 \times 10^{-20}$
EST3-EST27405-2	5.94	0	$340 \times 10^{-4}$	$120 \times 10^{-20}$

### I. Superposition of the nanoscale and of the percolating part of the mesoscale pore structures

The superposition of the nano- and mesopores is performed as follows. Let  $Z_n(\mathbf{x})$  be the phase function of the nanopores, i.e.,

$$\begin{aligned} Z_n(\mathbf{x}) &= 1 && \text{if } \mathbf{x} \text{ belongs to a nanopore} \\ &= 0 && \text{otherwise.} \end{aligned} \quad (11)$$

Let  $Z_m(\mathbf{x})$  be the phase function of the mesopores with a definition analogous to the previous one. Then, the nanopores and the mesopores are superposed. More precisely, the resulting solid phase is the intersection of the nano and the meso solid phases. Hence,  $Z(\mathbf{x})$ , the phase function of the superposition, is given by

$$1 - Z(\mathbf{x}) = [1 - Z_n(\mathbf{x})][1 - Z_m(\mathbf{x})] \quad (12a)$$

or, equivalently,

$$Z(\mathbf{x}) = Z_n(\mathbf{x}) + Z_m(\mathbf{x}) - Z_n(\mathbf{x})Z_m(\mathbf{x}). \quad (12b)$$

A first series of calculations was performed as follows. A small part of the percolating structure of the sample EST2-EST27405-1 was selected as displayed in Fig. 8(a). It should be reminded that this is a cracked mesoscopic sample. First, it is rediscrretized in voxels of size  $a = 2.12$  nm and mirrored with respect to the  $xy$  plane. Then, it is superposed to the reconstructed nanostructures which were described in Sec. A [see Fig. 8(b)]. The total porosity and the open porosity, which is equivalent to the percolating porosity, are systematically

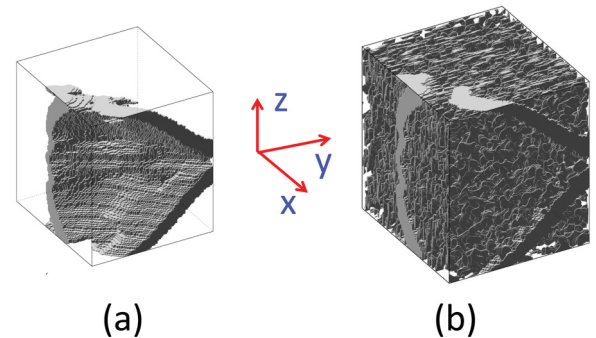


FIG. 8. Superposition of the nano- and of the percolating mesoscale structures.  $a = 2.12$  nm. (a) Part of EST2-EST27405-1. (b) Superposition with a nanoscale structure with a porosity equal to 14.2%.

TABLE VI. Superposition of the nanoscale and of the percolating mesoscale structure (a subsample of EST2-EST27405-1 illustrated in Fig. 9).  $a = 2.12$  nm.

$\varepsilon_n$	Percolation	Total porosity	Open porosity	$K'_{nmzz}$	$K_{nmzz}$ (m <sup>2</sup> )
0.102	0 y z	0.200	0.147	3.87	$1.74 \times 10^{-17}$
0.130	0 y z	0.225	0.199	3.90	$1.75 \times 10^{-17}$
0.142	x y z	0.236	0.218	3.92	$1.76 \times 10^{-17}$
0.200	x y z	0.288	0.282	4.02	$1.81 \times 10^{-17}$
0.252	x y z	0.334	0.332	4.14	$1.86 \times 10^{-17}$

determined and the permeability calculations are done only on this latter portion of the pore space.

The results are gathered in Table VI. For low-nanoscale porosities, the open porosity is very different from the total porosity. For high-nanoscale porosities, the two values are very close, which means that most of the porosity is connected.

The dimensionless permeability  $K'_{mzz}$  of the mesoporosity alone in the subsample displayed in Fig. 8(a) is equal to 3.77; the corresponding dimensional permeability  $K_{mzz}$  is equal to  $1.7 \times 10^{-18}$  m<sup>2</sup>. For  $\varepsilon_n = 0.102$ , the resulting permeability  $K'_{nmzz}$  is equal to 3.87 and therefore very close to  $K'_{mzz}$ . For larger values of  $\varepsilon_n$ , the differences are more significant, but the order of magnitude remains the same, and the difference between  $K_{nmzz}$  and  $K_{mzz}$  is very limited.

In dimensional terms, the permeabilities vary between  $1.7 \times 10^{-17}$  and  $1.9 \times 10^{-17}$  m<sup>2</sup>. These values are large, but they are consistent with the fact that the sample is cracked.

Since this subsample illustrated in Fig. 8(a) is very small, a larger portion was selected in the same EST2-EST27405-1 sample and it is displayed in Fig. 9(a); the size of this portion was chosen to be compatible with our computing possibilities which are of the order of  $10^6$  voxels. Now, the initial voxel size  $a = 8.48$  nm is kept and the nanostructure is generated with this value, and therefore with dimensionless correlation lengths equal to (1.5, 12.5, 12.5) in correspondance with what has been done before [see Fig. 9(b)]; this coarse discretization does not seem to influence the appearance of the nanostructure.

The dimensionless permeability  $K'_{mzz}$  of the mesoscopic pore volume alone is equal to  $0.133 \times 10^{-1}$ . The dimensionless permeability  $K'_{nzz}$  of the nanoscopic pore volume of porosity

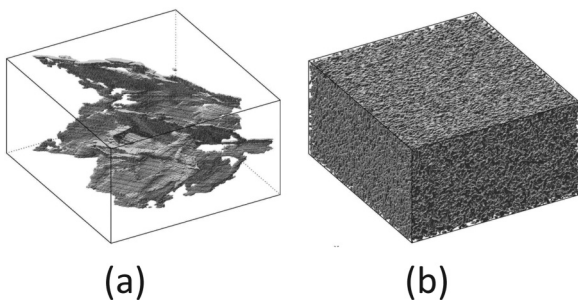


FIG. 9. Superposition of the nano- and of the percolating mesoscale structures.  $a = 8.48$  nm. (a) part of EST2-EST27405-1. (b) Superposition with a nanoscale structure with a porosity equal to 20%. Dimensionless correlation lengths are equal to (1.5, 12.5, 12.5) in correspondance with what has been done before.

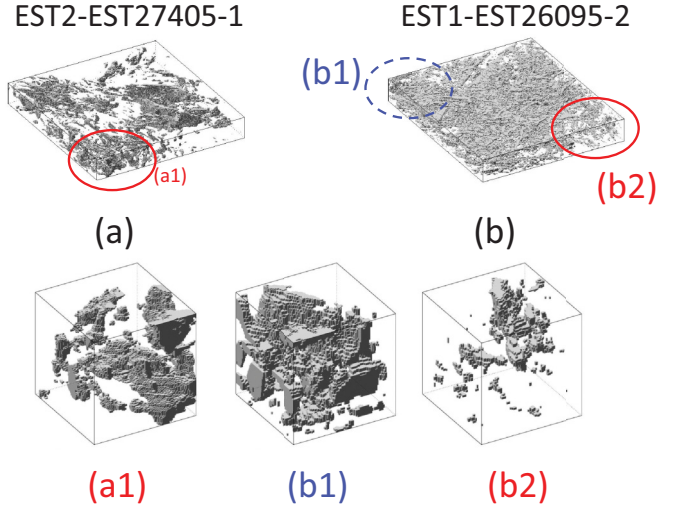


FIG. 10. Superposition of the nano- and of the total mesoscale structures.  $a = 2.12$  nm. The portion (a1) of EST2-EST27405-1 is nonpercolating. The portions (b1) and (b2) of EST1-EST26095-2 are percolating and nonpercolating, respectively. The portion (b1) is mirrored along the  $z$  axis in order to avoid bias in the determination of permeability.

0.2 alone is equal to  $0.489 \times 10^{-2}$ ; it should be compared with the permeability calculated with a voxel size equal to 2.12 nm; therefore, it should be multiplied by a factor 4 and it yields 0.0196 to be compared to 0.0132 (see Table IV); this discrepancy shows the necessity of a fine discretization for a good precision, but the orders of magnitude are kept. When the meso- and nanostructures are combined, the overall and open porosities are equal to 0.222 and 0.213, respectively. The dimensionless permeability  $K'_{nmzz}$  is equal to  $0.236 \times 10^{-1}$ , which is this time significantly greater than  $K'_{mzz}$  alone; the corresponding dimensional value is equal to  $1.7 \times 10^{-18}$  m<sup>2</sup>. Therefore, the nanopores cannot be neglected to estimate the overall permeability of the NS shale.

## 2. Role of the nonconnected mesoporosity

In the two previous examples, only the connected mesoporosity was considered. In this subsection, the role and the interaction of the complete mesoporosity with the nanoporosity is investigated. Two samples and three subsamples were selected as sketched in Fig. 10. The portion (a1) of EST2-EST27405-1 is nonpercolating. The portions (b1) and (b2) of EST1-EST26095-2 are percolating along the  $z$  axis and nonpercolating, respectively. All these subsamples are re-discretized with  $a = 2.12$  nm. The portion (b1) is mirrored along the  $z$  axis in order to avoid bias in the permeability determination. This mirroring operation is useless for (a1) and (b2) since the nanostructure is spatially periodic.

Results are displayed in Table VII, to which the dimensionless permeability  $K'_{b1mzz} = 0.503$  of subsample (b1) alone should be added. The first important feature in this table is that the permeability of the percolating sample (b1) superposed to the nanoporosity is always larger than the permeability of the other samples by at least one order of magnitude. The second important feature is that the nanoporosity does not influence

TABLE VII. Superposition of the nanoscale and of the total mesoscale structure.  $a = 2.12$  nm. The portion (a1) of EST2-EST27405-1 is nonpercolating. The portions (b1) and (b2) of EST1-EST26095-2 are percolating and nonpercolating, respectively.

Nano		EST2-27405-1		(b1)		(b2)	
$\epsilon$	$K'_{zz}$	$\epsilon$	$K'_{zz}$	$\epsilon$	$K'_{zz}$	$\epsilon$	$K'_{zz}$
0.130	$0.677 \times 10^{-3}$	0.196	$0.487 \times 10^{-2}$	0.252	0.580	0.157	$0.166 \times 10^{-2}$
0.142	$0.137 \times 10^{-2}$	0.207	$0.843 \times 10^{-2}$	0.261	0.594	0.169	$0.290 \times 10^{-2}$
0.200	$0.132 \times 10^{-1}$	0.260	$0.408 \times 10^{-1}$	0.310	0.691	0.225	$0.188 \times 10^{-1}$
0.250	$0.392 \times 10^{-1}$	0.308	$0.988 \times 10^{-1}$	0.355	0.820	0.275	$0.505 \times 10^{-1}$

much the permeability of (b1), since it varies between 0.503 (for  $\epsilon_n = 0$ ) and 0.820 (for  $\epsilon_n = 0.250$ ). This is not true for the permeability of the nonpercolating subsamples (a1) and (b2) which varies by an order of magnitude when  $\epsilon_n$  increases from 0.130 to 0.250.

If we go back to dimensional values, when the mesoporosity is percolating, then the permeability is of the order of  $2 \times 10^{-18}$  m<sup>2</sup>, while it is of the order of  $4 \times 10^{-20}$  m<sup>2</sup> for nonpercolating mesoporosities.

#### D. Permeability on the macroscopic scale

This permeability is determined by solving the elliptic equation (8) on a synthetic 3D medium obtained by the direct sampling method [14] from actual microtomography images of the same shale as in Ref. [7]. The medium is schematized by three phases. Phase 1 corresponds to the macropores (volume percentage 0.5), with an infinite permeability  $K_{\text{pore}} = \infty$ ; Phase 2 corresponds to the porous clay matrix, with a volume percentage of 60 and a permeability  $K_{nm0}$  given by the previous simulations; Phase 3 consists of the nonporous minerals, with a volume percentage of 39.5 and zero permeability  $K_{\text{nonporous}} = 0$ .

In principle, the Stokes equation should be solved in the macropores as it was done for the nano and mesopores. For practical reasons, the physical situation was simplified and the macropores were replaced by regions where the local permeability is large with respect to  $K_{nm0}$ . A dimensionless permeability  $K''$  is defined by

$$K''(\mathbf{x}) = \frac{K_M(\mathbf{x})}{K_{nm0}}. \quad (13a)$$

It takes the following values:

$$K''(\mathbf{x}) = \kappa_p \text{ in Phase 1, } 1 \text{ in Phase 2, } 0 \text{ in Phase 3,} \quad (13b)$$

where  $\kappa_p \gg 1$  is the dimensionless value of the local permeability in the macropores. Since the elliptic equation (8) as well as its boundary conditions are linear,  $K_M(\mathbf{x})$  can be replaced by  $K''(\mathbf{x})$  and the equation solved. The resulting dimensionless permeability  $\bar{K}''$  obtained by the Darcy equation (9) can be used to derive the dimensional macroscopic permeability  $K_{MA}$ ,

$$K_{MA} = K_{nm0} \bar{K}'' . \quad (14)$$

Several resolutions of (8) were done with  $\kappa_p = 0, 1, 10, 10^2, 10^3, 10^4, \text{ and } 10^5$ . For instance, for  $\kappa_p = 10^5$ , the permeability

tensor is equal to

$$\bar{\mathbf{K}}'' = \begin{pmatrix} 0.422 & 0.00645 & -0.00391 \\ 0.00381 & 0.375 & -0.00305 \\ -0.00317 & -0.00156 & 0.424 \end{pmatrix}. \quad (15)$$

$\bar{\mathbf{K}}''$  is close to spherical since the off-diagonal components are smaller than the diagonal ones by about two orders of magnitude and since the diagonal components are close to one another. This means that the medium is relatively isotropic. These observations were verified for all the values of  $\kappa_p$ . Therefore, the third of the trace was systematically derived for the various values of  $\kappa_p$ ,

$$\frac{\bar{K}''_{xx} + \bar{K}''_{yy} + \bar{K}''_{zz}}{3} = 0.372, 0.377, 0.389, 0.401, 0.405, 0.406, 0.407. \quad (16)$$

Since the macropores have a small probability, their influence on the overall permeability is weak, hardly 10%, when  $\kappa_p$  varies from 0 up to infinity. The influence of the impermeable phases is larger and therefore the dimensionless macroscopic permeability can be approximated by

$$\bar{K}'' = 0.41. \quad (17)$$

This is a value slightly smaller than the probability of the porous clay matrix in the sample which is equal to 0.6.

## IV. DISCUSSION

Most of the results obtained in Sec. III are displayed in Fig. 11. They clearly gather into two groups. The lower permeabilities are obtained when the mesoporosity does not percolate, in which case the permeability is of the order of the nanoscale permeability  $K_n$ . The larger permeabilities are obtained when the mesoscale porosity percolates; they are then close to the mesoscale permeability.

These observations are consistent with Ref. [23] and Ref. [27]. When two porous structures 1 and 2 with two very different permeabilities  $K_1 \ll K_2$  are mixed, the permeability  $K_w$  of the whole can be schematized as follows. If the porous structure 2 percolates, then  $K_w$  is close to  $K_2$ ; when the porous structure 2 does not percolate,  $K_w$  is close to  $K_1$ .

Another question is that of the representativeness of the permeability predictions at the macroscopic scale. Due to the limited nanoscale and mesoscale sample sizes, the permeability provided at the macrocale is not representative in a deterministic sense. Rather, we have provided a range of nanoscale pore structures, with varying porosity (10 to 25.2%),

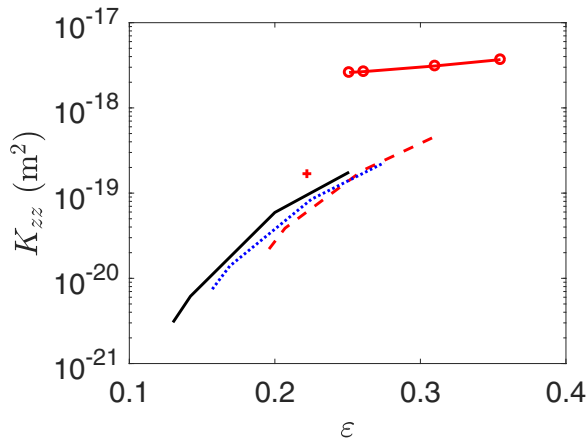


FIG. 11. Dimensional permeability. Superposition of the nanoscale and of the total mesoscale structures. Data are for nanoporosity (solid black line), nanoporosity and nonpercolating mesoporosity (a1) (blue dotted line), nanoporosity and nonpercolating mesoporosity (b2) (red broken line), nanoporosity and percolating mesoporosity (b1) (red solid line with  $\circ$ ), sample displayed in Fig. 9 (red cross).

another range of 3D pore structures at the mesoscale (by FIB-SEM imaging), and, finally, a macroscale sample of  $1 \text{ mm}^3$  involving all the mineral phases possibly present in NS (and bigger than the original micro CT images). Representativeness is achieved in a statistical sense, where a range of macroscopic permeability values is provided, in relation to the variability of the pore structure at the two main scales where it is present (nano and mesoscales). For undisturbed NS,

$$3 \times 10^{-21} \text{ m}^2 \leq K_{MAyy} \simeq K_{MAzz} \leq 1.8 \times 10^{-19} \text{ m}^2. \quad (18)$$

For NS cracked at the mesoscale,

$$2.8 \times 10^{-19} \text{ m}^2 \leq K_{MAyy} \simeq K_{MAzz} \leq 1.9 \times 10^{-17} \text{ m}^2. \quad (19)$$

With 2D TEM imaging, the anisotropy of the shale is not preponderant over other parameters such as pore connectivity at the mesoscale or the presence of microcracks.

These estimations are consistent with experimental measurements at the centimetric scale for undamaged NS shale, where  $K_{\text{exp}}$  varies between  $8 \times 10^{-21} \text{ m}^2$  and  $6 \times 10^{-20} \text{ m}^2$ , when measured with a neutral liquid fluid such as ethanol [8] [cf. (1)]. When the size of the explored zones by FIB-SEM and TEM is compared to the overall size of the sample, the agreement is satisfactory.

## V. CONCLUDING REMARKS

Compared to the mesoscopic permeability  $K_{nm}$  of the combined nanoscopic and mesoscopic pore structures, the macroscopic permeability represents 40%, i.e., it is of the same order of magnitude, although smaller. This means that small scale pore structures actually drive the fluid transport through the shale. Our calculations show that the contribution of the nanoscopic pore structure cannot be neglected when assessing the transport of undisturbed matter. However, whenever the shale is cracked at the mesoscale, the permeability  $K_{nm}$  is of the same order as  $K_m$ , i.e., the nanoscopic pore structure can be neglected for assessing fluid transport. This should be similar when discussing gas migration through liquid-saturated shale; cracks, when present, are bound to drive gas transport. However, it is expected that such conclusion cannot be drawn for other phenomena relating to these shales, i.e., gas transport, water sorption/desorption, ion diffusion, etc.

## ACKNOWLEDGMENTS

We acknowledge funding by NEEDS MIPOR (Grand Défi Inter-Disciplinaire Nucléaire: Energie, Environnement, Déchets, Société-Milieus POREux, funded by CNRS, CEA, EDF, ANDRA, AREVA, IRSN, BRGM, France) in 2016, under the PERMEARGILE project label. The SEM and TEM national facilities available at the Centre Commun de Microscopie de Lille (France) are supported by the Conseil Régional du Nord-Pas de Calais and by the European Regional Development Fund (ERDF). Part of this work was performed when P. M. Adler was supported at the Mechanical Engineering Department, Technion, Haifa, Israel, by a fellowship of the Lady Davis Foundation.

- 
- [1] B. Felix, and P. Lebon, R. Miguez, and F. Plas, *Eng. Geol.* **41**, 35 (1996).
- [2] M. E. Curtis, R. J. Ambrose, C. H. Sondergeld, and C. S. Rai, in *Proceedings of the Canadian Unconventional Resources and International Petroleum Conference, Calgary, Alberta, Canada*, SPE-137693-MS (Society of Petroleum Engineers, London, UK, 2010).
- [3] P. Marschall, S. Horseman, and Th. Gimmi, *Oil Gas Sci. Technol.* **60**, 121 (2005).
- [4] L. M. Keller, L. Holzer, R. Wepf, and P. Gasser, *Appl. Clay Sci.* **52**, 85 (2011).
- [5] L. M. Keller, L. Holzer, R. Wepf, P. Gasser, B. Munch, and P. Marschall, *Phys. Chem. Earth* **36**, 1539 (2011).
- [6] L. M. Keller, P. Schuetz, R. Erni, and M. D. Rossell, F. Lucas, M. Lucas, P. Gasser, and L. Holzer, *Micropor. Mesopor. Mater.* **170**, 83 (2013).
- [7] J. C. Robinet, P. Sardini, D. Coelho, J. C. Parneix, D. Prêt, S. Sammartino, E. Boller, and S. Altmann, *Water Resour. Res.* **48**, (2012).
- [8] Y. Song, C. A. Davy, D. Troadec, A.-M. Blanchenet, F. Skoczylas, J. Talandier, and J.-C. Robinet, *Mar. Pet. Geol.* **65**, 63 (2015).
- [9] Y. Song, C. A. Davy, P. Bertier, and D. Troadec, *Micropor. Mesopor. Mater.* **228**, 64 (2016).
- [10] Y. Song, C. A. Davy, and D. Troadec, *Oil Gas Sci. Technol.* **71**, 51 (2016).

- [11] B. Yven, S. Sammartino, Y. Géraud, F. Homand, and F. Villieras, *Mém. Soc. Géol. France* **178**, 73 (2007).
- [12] J. K. Mitchell, *Fundamentals of Soil Behavior*, 2nd ed. (John Wiley & Sons, New York, 1993).
- [13] C. L. Zhang and T. Rothfuchs, *Appl. Clay Sci.* **26**, 325 (2004).
- [14] T. N. Kim, *Direct Sampling Applied to Porous Media*, Ph.D. thesis, Universit Pierre et Marie Curie (2013).
- [15] G. Mariethoz, P. Renard, and J. Straubhaar, *Water Resour. Res.* **46**, (2010).
- [16] J. Koplik and J. R. Banavar, *Annu. Rev. Fluid Mech.* **27**, 257 (1995).
- [17] A. Pazdniakou and P. M. Adler, *Adv. Water Res.* **62**, 292 (2013).
- [18] A. Henriette, C. G. Jacquin, and P. M. Adler, *Phys. Chem. Hydrodynam.* **11**, 63 (1989).
- [19] J. C. Robinet, P. Sardini, M. Siitari-Kauppi, D. Prêt, and B. Yven, *Sediment. Geol.* **321**, 1 (2015).
- [20] Y. Song, C. A. Davy, P. Bertier, F. Skoczylas, and J. Talandier, *Micropor. Mesopor. Mater.* **239**, 272 (2017).
- [21] J.-F. Thovert, J. Sallès, and P. M. Adler, *J. Microsc.* **170**, 65 (1993).
- [22] P. M. Adler, C. G. Jacquin, and J. A. Quiblier, *Int. J. Multiphase Flow* **16**, 691 (1990).
- [23] A. Moctezuma-Berthier, O. Vizika, J.-F. Thovert, and P. M. Adler, *Transp. Porous Media* **56**, 225 (2004).
- [24] M. Khamforoush, K. Shams, J.-F. Thovert, and P. M. Adler, *Phys. Rev. E* **77**, 056307 (2008).
- [25] S. Melchionna and U. M. B. Marconi, *Europhys. Lett.* **81**, 34001 (2008).
- [26] E. I. Wachspress, *Iterative Solution of Elliptic Systems* (Prentice Hall, New York, 1965).
- [27] I. I. Bogdanov, V. V. Mourzenko, J.-F. Thovert, and P. M. Adler, *Water Resour. Res.* **39**, 1023 (2003).